Diamond detector with laser-formed buried graphitic electrodes: micron-scale mapping of stress and charge collection efficiency

S. Salvatori, *Member, IEEE*, M.C. Rossi, G. Conte, T.V. Kononenko, M.S. Komlenok, A.A. Khomich, V.G. Ralchenko, V.I. Konov, G. Provatas, and M. Jaksic

***Abstract*—The paper reports the micron-scale investigation of an all-carbon detector based on synthetic single crystal CVD-diamond having an array of cylindrical graphitic buried-contacts, about 20 μm in diameter each, connected at the front side by superficial graphitic strips. To induce diamond-to-graphite transformation on both detector surface and bulk volume, direct-laser-writing technique was used. Laser-treatment parameters and cell shape have been chosen to minimize the overlapping of laser-induced stressed volumes. Optical microscopy with crossed polarizers highlighted the presence of an optical anisotropy of the treated material surrounding the embedded graphitized columns, and non-uniform stress in the buried zones being confirmed with a confocal Raman spectroscopy mapping. Dark current-voltage characterization highlights the presence of a field-assisted detrapping transport mainly related to highly-stresses regions surrounding buried columns, as well as superficial graphitized strips edges, where electric field strength is more intense, too. Notwithstanding the strain and electronic-active defects, the detector demonstrated a good charge collection produced by 3.0 and 4.5 MeV protons impinging the diamond, as well as those generated by MeV β-particles emitted by ^{90}Sr source. Indeed, the mapping of charge collection efficiency with Ion Beam Induced Charge technique displayed that only a few micrometers thick radial region surrounding graphitic electrodes has a reduced efficiency, while most of the device volume preserves good detection properties with a charge collection efficiency around 90% at 60 V of biasing. Moreover, a charge collection efficiency of 96% was estimated under MeV electrons irradiation, indicating the good detection activity along the buried columns depth.**

***Index Terms*—3D detectors, β-particles, graphitic pillars, IBIC, protons, sc-CVD diamond**

I. Introduction

Silicon and germanium have been considered for many years the elective semiconductor materials for radiation and particle detectors fabrication. However, such tetravalent semiconductors depict a low tolerance to radiation damage and devices are less stable either in harsh conditions or under high-energy particle fluences when compared to diamond based detectors [1-2]. Although diamond is considered as one of the best radiation-tolerant material, yet the diamond detectors show a certain degradation in terms of their detectivity upon operation under very high radiation fluences [3]. To overcome such a detrimental effect, several research groups implemented in diamond three-dimensional contact structures (an array of conductive wires embedded in bulk of the crystal) similar to those proposed for Si and GaAs based detectors [4] aimed at improving the Charge Collection Efficiency (CCE) of generated carriers. The use of such a 3D-design leads to several advantages in comparison with conventional planar electrode system, due to a possible drastic reduction of the distance between contacts: a shorter drift path of generated carriers assures a lower probability of charge trapping, guaranteeing good response even after long irradiation periods; higher electric field strengths can be achieved at lower values of the applied voltage. For diamond, buried contacts can be realized by means of either focused ion beams (also named Deep Ion Beam Lithography, DIBL) [5-7] or pulsed-laser treatments [8]. Those two techniques are adopted to induce a local transformation of insulating diamond into conductive graphite, hence device contact realization, also acting as distributed electrodes within the bulk material and/or on diamond surface.

The laser-induced local transformation of diamond into graphite represents a powerful tool used for the development 3D-contacts devices [9-13], all-carbon detectors [14-15], graphite resistors on diamond [16] (opening the way to redesign position sensitive devices based on distributed resistive superficial contacts [17]), as well as the realization of complex three-dimensional geometries [18]. Several research groups reported detailed investigations on their experimental process conditions [19-21], mainly studied to: increase the buried contact aspect-ratio (length over diameter) in order to decrease contacts' distance for the same detector active volume; assure a good buried-contact conductivity by optimizing laser-treatment parameters (power-density, scan velocity, repetition rate) experimenting with either nanosecond, picosecond or femtosecond pulsed laser sources. However, graphitic paths are strongly process-dependent and a proper choice of laser-treatment parameters is fundamental for the realization of high quality contacts in device fabrication. For example, on a micrometer scale, a buried laser-generated graphitic column is

Paper submitted on 2019-02-08; revised July 12, 2019.
This work was supported in part by Russian Ministry of Education and Science (Project 3.2608.2017/4.6). Measurements at RBI have had the support of project AIDA-2020, GA no. 654168.
S. Salvatori is with the Università Niccolò Cusano, Via don Carlo Gnocchi 3 - 00166 Rome, Italy (e-mail: stefano.salvatori@unicusano.it). M.C. Rossi and G. Conte are with the Università Roma Tre, Via V. Volterra 62 - 00146 Rome, Italy (email: mariacristina.rossi@uniroma3.it, gconte@fis.uniroma3.it). T.V. Kononenko, M.S. Komlenok, A.A. Khomich, V.G. Ralchenko and V.I. Konov are with Prokhorov General Physics Institute, of the Russian Academy of Sciences, Vavilova 38 - 119991 Moscow, Russia (e.mail: taras.kononenko@nsc.gpi.ru, komlenok@nsc.gpi.ru; antares-610@yandex.ru; vg_ralchenko@mail.ru; vik@nsc.gpi.ru). G. Provatas and M. Jaksic are with the Ruder Boskovic Institute Bijenicka cesta 54 - 10000 Zagreb, Croatia (email: Georgios.Provatas@irb.hr; jaksic@irb.hr).

far from an ideal cylinder and its geometry looks like a kind of a tree with thin branches spreading out not only along the laser beam direction, but also fanning out from the central body of the column, with the sp^3 to sp^2 ratio strongly dependent on the laser parameters [19, 22]. Lagomarsino et al. [22] reported a significant difference in morphology and electrical conductance of the buried graphitic structures fabricated by nanosecond- and femtosecond-pulsed laser radiation, with a more defective layers formed around the ns-columns. The stress [21-24] and defects, such as 3H defect (carbon interstitial) [25], appear around the graphitic pillars, and this should have a direct impact on local electronic properties of diamond. Sotillo et al. [24] applied polarized confocal Raman spectroscopy to study the origin of stress-induced waveguides in diamond, produced by femtosecond laser writing. They mapped the stress and the refractive index in a gap between adjacent buried graphitic wires arranged in close proximity to each other, on a scale of the order of 10 μm, and revealed a co-existence of tensile and compressive stress in different orientations. Salter et al. [26] studied the internal structure of fs-laser induced graphitic wires using TEM and electron energy loss spectroscopy and revealed multiple micro-cracks and nano-clusters of sp^2 bonded carbon embedded into sp^3 bonded diamond matrix. Ashikkalieva et al. [19] applied scanning spreading resistance microscopy to investigate spatial arrangement of sp^2 bonded nano-sheets forming conductive network inside wires. Forcolin et al. [21] used the proton microbeam to map local charge collection efficiency (CCE) with Ion Beam Induced Charge (IBIC) technique for fs-laser induced buried graphitic electrodes array. However, as the stress field was not quantified, no direct comparison of the stress and CCE maps for diamond around the electrodes, was documented.

In the present work we realized an array of buried graphitic columns in a single crystal CVD-diamond slab by means of femtosecond infrared laser, and analyzed on micron-scale the spatial distributions of stress and local charge collection efficiency of the pillared device, in the vicinity and between the graphitic electrodes, in order to establish a correlation between the damage (stress) level of the material and its electronic properties and detection capability. Graphitized superficial strips and pads, obtained applying a similar laser-treatment apparatus with ArF source, were used to define the overall detector contact geometry. Aiming at preserve the good electronic quality of the pristine diamond sample, in comparison to other investigated cell-shapes [9, 13, 27], the laser-formed buried contacts geometry of the detector was designed to minimize the overlapping between stressed regions originated by the laser-treatment itself, which mainly propagates along the {111} crystal direction [19].

To investigate the presence of lattice defects like those already evidenced in previous devices [25], as well as strained regions surrounding the pillar itself, we used microRaman analysis and dark field polarized optical microscopy. Ion Beam Induced Charge (IBIC) imaging with 3 and 4.5 MeV protons micro-beam was used to estimate the detection performance of the device, whereas high-energy β-particles emitted by a ^{90}Sr source were used to evaluate the charge collection efficiency along the detector thickness defined by the buried-pillars depth. Current-voltage measurements have been also used to investigate the effects of stress and defects induced by laser-treatment on the detector dark conductivity highlighting the presence of a field-assisted detrapping process in the charge carriers transport mechanism, which dominates at higher applied voltages.

II. Experimental details

A. Material and detector fabrication

A single crystal (100)-oriented "detector grade" CVD diamond 3×3 mm^2 plate from Element Six™ with nitrogen and boron impurity content lower than 5 ppb and 1 ppb, respectively, as claimed by the producer [28], was used in this work. Using standard mechanical procedures, all surfaces of the plate were mechanically polished for final dimensions around 3×3×0.47 mm^3. (The four lateral faces were polished allowing visual inspection during the subsequent laser-process graphitization for buried-pillars fabrication.) To remove polishing residuals, the sample was then dipped in hot chromic acid solution followed by aqua regia, finally rinsed in hot DI water and in isopropanol.

For laser treatment, a computer controlled three-axis translation stage was used to hold the diamond plate precisely moved with respect to the laser beam focal point (position tolerance and repeatability better than ±10 μm). A femtosecond VaryDisc50 laser (Dausinger + Giesen GmbH), operated at 1030 nm, with 400 fs of pulse duration and 200 kHz of pulse-repetition-rate, was applied for diamond-to-graphite local transformation [29]. Graphitized regions formation during the laser process was observed by means of a CCD camera coupled to a ×20 microscope objective located perpendicularly to the laser beam direction.

Both the laser-pulse energy and the scan speed represent fundamental parameters for a proper device fabrication. The former was set at about 0.5 μJ and graphitic columns were induced by moving the sample along the beam direction at a constant speed of 50 μm/s. Resulting pillars were 20 μm in diameter having a regular shape along the scan direction. As shown in Fig. 1(a), we adopted the same buried contacts geometry depicted in ref. [29], composed by an array of "elementary cells" with dimensions x = 150 μm and y = 300 μm. Compared to that used in ref. [30], a buried columns distance d around 170 μm was preferred to maintain an adequate drift distance of charge carriers at few tens of Volts of applied bias. The rectangular face-centered cell (partially resembling a hexagonal shape [27]) adopted for the device would assure a minimized overlapping of laser-induced stressed regions mainly localized within the {111} planes [19, 31], although this appears particularly important for relatively low d distance in micrometer range.

Each buried graphitic contact, about 370 μm long (in depth, see Fig. 1(b)), was produced in a single laser-irradiation step along the [001] crystal direction. Columns height within the bulk, maintained 100 μm lower than diamond sample thickness, assured the presence of an insulating layer at the back of

This article has been accepted for publication in a future issue of this journal, but has not been fully edited. Content may change prior to final publication. Citation information: DOI 10.1109/JSEN.2019.2939618, IEEE Sensors Journal

the device. In addition, compared to previous works [29, 30], laser-process adopted in the present work allowed to fabricate well-defined buried columns with a relatively low tolerance of ±2% in height.

The produced graphitic columns then were connected by superficial interdigitated graphitic strips on the polished sample front side, ~50 μm wide, ~10 μm thick, and 150 μm apart, formed with an excimer ArF laser (λ = 193 nm). The strips were obtained by 25% overlapping of 50×50 μm^2 square spots with uniform laser fluence of 5 J/cm^2. By current-voltage measurements of such superficial graphite strips (by means of a Keithley 6517A), we evaluated a resistivity around 0.16 ± 0.02 Ω cm, whereas a value around 0.5 Ω cm is estimated for buried columns [19]. Finally, to simplify external device connections, two lateral graphitized 2.5×0.35 mm^2 rectangular pads were realized on two opposite 3×0.47 mm^2 lateral faces (see Fig. 1) by means of the mentioned excimer laser apparatus. Fig. 2 shows the photograph of the realized detector.

Single component cyan-acrylic liquid glue was used to fix the device to a single-face Printed Circuit Board (PCB) having two copper traces "soldered" to the lateral graphitic contacts by means of silver paste. The PCB, used for device connection to the front-end and signal acquisition electronics, as well as detector biasing, allowed the irradiation also on the back side of the detector thanks to the presence of a 2 mm hole centered to the diamond die.

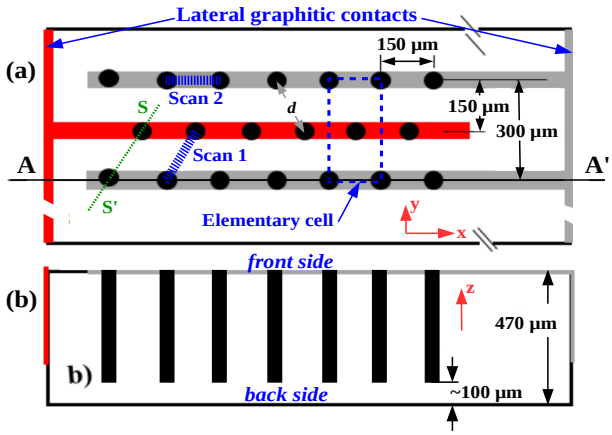

Fig. 1 Layout of the 3D-contacts detector: (a) front view of a part on the surface with graphite strips connecting buried columns. *d* represents the contact distance between two polarized nearest neighbor pillars. "Scan #" illustrates the directions in Raman analysis. Dotted rectangle represents the area identifying a detector "elementary-cell"; (b) cross-sectional (A-A') view of the buried-contacts structure with end 100 μm apart the sample back side.

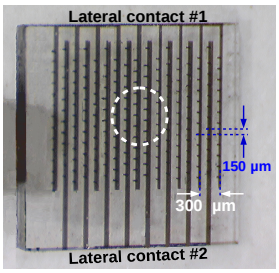

Fig. 2 Micrograph of the diamond detector (top view). Dotted circle depicts the detector area where approximately impinges the collimated β-particles beam (see text for details).

B. Optical microscopy and Raman spectroscopy

A Nikon Eclipse 50LPol microscope equipped with crossed polarizer and analyzer (black field) and a Nikon Ds-Fi1 color camera were used to investigate the optical anisotropy distribution induced by buried columns fabrication. The focal plane of a 4×/0.13 achromatic objective was maintained on the front sample surface, whereas the polarization axis was initially set parallel to the superficial graphitic strips, *i.e.* to the <110> crystal orientation.

For Raman analysis, a Jobin-Yvon LabRam HR800 spectrometer in a confocal configuration with spatial resolution of about 1 μm, at an excitation wavelength of 473 nm, was used. The laser beam was focused either on the sample front surface or within the bulk, and the scattered light was collected in a back-scattering geometry using an Olympus microscope objective (100×, N.A. = 0.90). The spectrometer calibration, in the same conditions used for diamond sample characterization, was performed using the 1st order Raman line of a high quality type IIa natural diamond, ν_{D0} = 1332.5 cm^{-1} with a FWHM of 1.6 cm^{-1}, used as reference.

C. Device characterization under MeV electrons

Beta particles, emitted from ^{90}Sr source (1 MBq, QSA Global, code SIFB13505, item 22/2006) which have a maximum energy of 2.28 MeV, have been used to measure the detector average charge collection over the bulk material. The ^{90}Sr source was hosted inside a 25 mm long brass cylinder with an aperture of 0.4 mm in diameter and 5 mm in depth. In such a condition, the output electron beam resulted quite well collimated with a relatively small divergence: β-particles are emitted within a solid angle around 5×10^{-3} sr. A natural diamond ADII-3 (UralAlmazInvest) fast detector (time resolution better than 1 ns) was used as trigger device and positioned 10 mm apart from the brass cylinder base (*i.e.* 15 mm from the β-source) and its front diaphragm (Ø = 1.5 mm) was aligned to the cited solid angle of ^{90}Sr emission. The CVD-diamond Detector Under Test (DUT) was then positioned in the middle between the β-source and the ADII-3 trigger and the center of its active detection area was aligned within the mentioned emission solid angle. In such a condition, β-particles mainly impinge on about 0.5 mm^2 of the detector active area (see dotted circle in Fig. 2). The adopted setup assured that high energy electrons emitted by ^{90}Sr source have to deposit enough energy in the ADII-3 detector to be accepted as an event by the acquisition system. Both DUT and trigger signals were preamplified by using two fast rise-time and low-noise hybrid Charge Sensitive Amplifiers (CSA), CAEN A1422H-F2 (45 mV/MeV in Si). A CAEN N6724a two-channels digitizer, 14 bit, 100 MS/s and 500 mV$_{pp}$ of dynamic range, was used for data collection and analysis using the CAEN DPP-PHA digital pulse processing software. The time acquisition window between the two channels was set to 10 ns. The performed amplitude calibration procedure is described elsewhere [29]. For device voltage biasing, a CAEN N1471A power supply was used. Finally, the trigger threshold during acquisitions was set to 0.2 fC, greater than the Gaussian noise amplitude evaluated with measurement in free-running mode (external trigger disabled).

D. IBIC characterization with MeV protons

We performed IBIC analysis with protons at Ruder Boskovic Institute in Zagreb using a Van-de-Graaff tandem accelerator [32]. The energy of the scanning micro-beam (focus smaller than 2 μm), was set at 3.0 and 4.5 MeV. The spatial distribution of the ionization charge, evaluated with SRIM code [33], indicates that, for the mentioned energies, protons stopping power in diamond is around 48 and 97 μm, respectively, so that they are completely absorbed within the detector volume. The readout chain consisted of a CSA (ORTEC 142A) followed by a shaping amplifier (ORTEC 570) with a shaping time of 2.0 μs. A dedicated beam scanning and data acquisition system displayed the signal values on 128×128 pixels images, reading the amplitude of the charge signal with a trigger threshold regulated to 10.000 electrons. A silicon barrier detector and a copper grid on the beam path was used to calibrate the readout chain by assuming an e-h pair production energy of 3.62 eV for silicon [34] while 13.0 eV was used to evaluate the pair production in diamond [35].

III. Results and Discussion

A. Optical microscopy analysis

Optical microscopy images were acquired in a dark-field condition. The image of Fig. 3(a) clearly shows the presence of wide bright regions distributed around a buried graphitic column (visible as a black dot of about 20 μm in diameter). These regions, extended for 50-80 μm from the pillar, highlight the presence of stress induced in the pristine crystal by volume expansion of the material converted to graphitic pillar. The maximum strain is concentrated along lines connecting nearest neighbor pillars, so the material compression is not isotropic, resulting in birefringence of the solid. Although the number of nearest neighbor pairs of buried columns is 6 (4 located at the cell corners and 2 belong to the same graphitic strip, see Fig. 1), Fig. 3(a) displays only 4 strain "lines" coming from the pillars forming the cell's corner: hidden vertical plumes in the figure are oriented along the forbidden polarization direction (<110> crystal orientation), and masked by superficial graphitic strips, too. In a smaller-scale of a few microns, Fig. 3(a) also shows the presence of colored contrast in proximity of each pillar, revealing a stress change surrounding the pillar surface, as further confirmed by Raman analysis. It is worth to note the symmetry of the colored patterns, homogeneously distributed along the pillar surrounding, obtained by a proper alignment of polarizers and the diamond crystal orientation. Isochromatic fringes could be compared with Michel Lévy table [36] to estimate the local refractive index variation if the retardation value and the diamond crystal thickness are known. Conversely, to simplify the analysis, assuming the brightness of the cross-polarized image to be proportional to the stress in diamond, the images can be used as relative measure of stress [21]. The profile of the brightness along the line connecting two neighbor electrodes is shown in Fig. 3(b) on log scale, which reveals a minimum of stress in the middle between the electrodes. In addition, a sharp increase of light intensity in the regions adjacent to the buried columns is also revealed, mainly attributed to the volume expansion of the laser-formed pillar. Both the two aspects are confirmed by Raman spectroscopy analysis as illustrated in the next section.

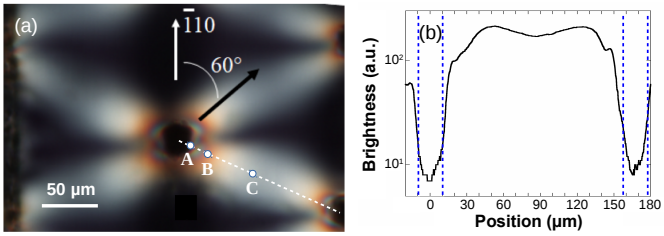

Fig. 3(a). Cross-polarizer optical microscopy image: graphite strips parallel to the polarization axis. Bright areas around the pillars highlight different degree of stress here evidenced as optical anisotropy. A, B, and C points indicate significant positions where Raman spectra were acquired (see text). (b) Brightness profile along the dashed white line in (a) connecting two neighboring electrodes. Vertical dotted lines show the pillars extension.

B. Raman analysis

Micro-Raman mapping along the line between two nearest neighbor graphitic pillars have been performed in order to gain an insight into vibrational scattering in different points close to the laser-treated volume, as well as the untreated region between two buried contacts. Significant results are summarized in Fig. 4 where Raman spectrum of pristine diamond is also reported for reference (dotted curve), displaying a single diamond peak at ν_{D0} = 1332.5 cm^{-1} with a FWHM of about 2 cm^{-1}, characteristic for high quality single crystal material. In contrast, in the spectrum *A*, acquired 10 μm apart from the pillar center (point 'A' of Fig. 3), diamond peak becomes asymmetric, splitting into three distinct singlet components at 1329, 1334, and 1339 cm^{-1}, respectively. The lower wavenumber component is found to downshifted, while the second and third ones are upshifted, suggesting a superposition of tensile and compressive stress components. Such a phenomenon reveals the presence of high anisotropic stress mainly located at the buried pillar boundary. At this time, we cannot ascertain the origin of these phonon modes and more work is needed to proper attribute the underlaying mechanism of stress formation.

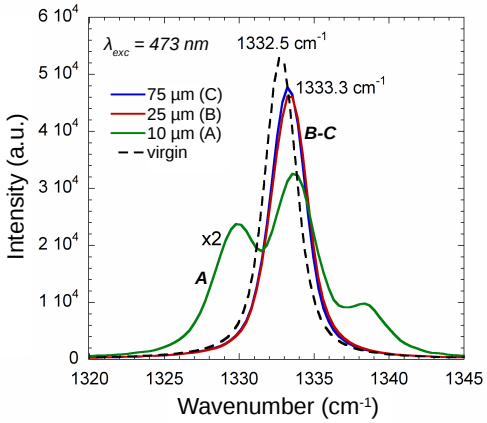

Fig. 4 Raman spectra at three different points: close the laser-treated zone (A and B), and in the middle between two buried pillars (C). A, B, and C refer to the points depicted in Fig. 3(a). Dotted curve refers to Raman spectrum of pristine diamond sample.

This article has been accepted for publication in a future issue of this journal, but has not been fully edited. Content may change prior to final publication. Citation information: DOI 10.1109/JSEN.2019.2939618, IEEE Sensors Journal

The Raman spectra acquired close to the pillar, but in the untreated volume (points 'B' of Fig. 3, 25 µm apart from the pillar center), and in the middle of the region between two pillars (point 'C', Fig. 3, 75 µm apart from the pillar center), respectively, depict a more intense diamond peak 1 cm^{-1} upshifted with respect to ν_{D0}, with unchanged FWHM of about 2 cm^{-1}. This suggests the occurrence of a structural relaxation to a compressive stress, where the cubic symmetry of diamond as well as crystalline order are preserved in the regions outside the laser-treated volumes.

More details on Raman spectra variations were revealed in scans performed along lines between two nearest neighbor pillars. Fig. 5 reports the 1st order diamond Raman peak position ν_D and FWHM value evaluated from spectra acquired every 5 µm along the bulk region between two pillars positioned on adjacent graphitic strips (*"scan 1"* line of Fig. 1). Analysis of the ν_D wavenumber highlights a significant change of the Raman spectra along the mapped line, which displays a strongly widened diamond peak (with FWHM up to 8.5 cm^{-1}), frequency shifted toward lower wavenumbers (up to 1.8 cm^{-1}), suggestive of a possible superposition of process related structural defects and tensile stress effects. Conversely, in the region between the two pillars, spectra highlight the existence of compressed (upshift of ν_D slightly lower than 1.0 cm^{-1}), but ordered crystal (indeed, peak width remains narrow, with FWHM = 2.0 cm^{-1}). For data depicted in Fig. 5, a corresponding compressive stress around 0.38 GPa is estimated by using the relationship $\sigma = 0.38\ (\nu_D - \nu_{D0})$ GPa [37]. Such a result is consistent with the decrease of plumes brightness in Fig. 3, region labeled 'C', suggesting a lowering of crystal compression in the central region between two pillars.

It is worth to note that Raman peak position and image brightness in the region between the two pillars appears fairly well correlated, as shown in Fig. 6. Using a line-shape fitting procedure we were able to detect small changes (< 0.1 cm^{-1}) in the diamond Raman peak position, which complement well the picture of cross-polarization optical microscopy. In the literature, the two techniques are reported as indirect stress evaluation tools [21, 38]. A behavior similar to that illustrated in Fig. 6 has been observed using polarized micro-Raman measurements [24] between closely spaced, laser written tracks, where a stress induced refractive index change is evidenced as responsible for optical guiding effect. Brightness data of Fig. 6 clearly show a strong decrease in the ~20 µm wide rings surrounding each pillar. Conversely, such regions would display the highest stress as highlighted by the diamond peak shift in the Raman analysis. Brightness decrease may be a consequence of "monochromatic" light selection induced by birefringence of the crystal. However, a more detailed investigation is needed on isochromatic fringes interpretation before a self consistent analysis can be carried out.

Plot of Fig. 7 shows an analysis similar to that illustrated in Fig. 5, but related to the scan along two pillars of the same graphitic strips (*"scan 2"* line of Fig. 1). Experimental data are quite similar to the previous ones: a Raman peak downshift and broadening detected in the pillar area and a ν_D upshift in

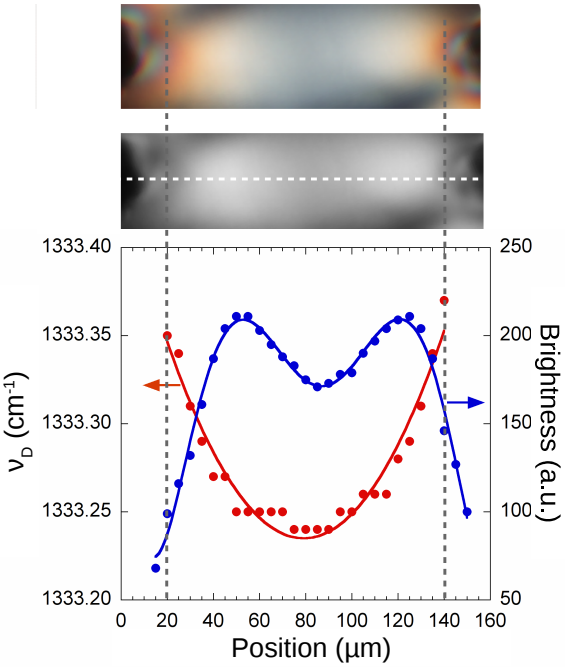

Fig. 6 Cross-polarizer optical microscopy image (top) and its corresponding images in gray tones (middle). Plot reports diamond peak position and brightness data vs. position along the dotted white line reported in the middle image. Vertical dotted lines indicate the position of maximum strain as highlighted by diamond peak shift in the Raman spectra.

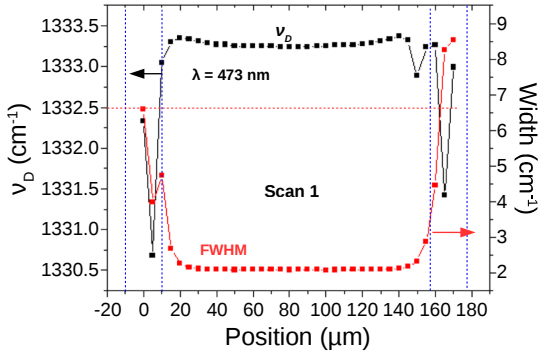

Fig. 5 Diamond peak position and FWHM evaluated from Raman spectra scanning the region between two pillars of two adjacent graphite strips (*"scan 1"* line in Fig. 1). The maximum upshift deviation from the reference value ν_{D0} = 1332.5 cm^{-1}, known for unstrained diamond, is lower than 1.0 cm^{-1} in the region between pillars where a constant FWHM is apparent.

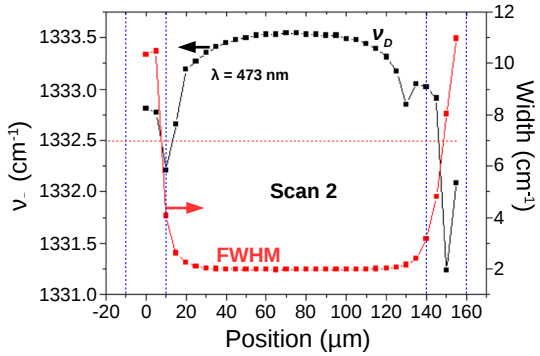

Fig. 7 Diamond peak position and FWHM evaluated from Raman spectra scanning the region between two pillars at the same superficial graphite strip (*"scan 2"* line in figure 1). The regions between dotted vertical lines represent the nominal buried contacts zones. Horizontal line at 1332.5 cm^{-1} corresponds to the Raman peak position for unstrained diamond.

This article has been accepted for publication in a future issue of this journal, but has not been fully edited. Content may change prior to final publication. Citation information: DOI 10.1109/JSEN.2019.2939618, IEEE Sensors Journal

the region between the pillars. However a slightly higher upshift (of about 1.2 cm^{-1}) is observed moving toward the region in the middle between two pillars. Such an effect can be tentatively attributed to an enhancement of compressive stress due to a lower distance between pillars of the same strip (150 µm) in comparison to that of pillars belonging two adjacent strips (about 170 µm), although a small compressive contribution induced by surface graphitic strips formation cannot be ruled out. Conversely, FWHM behavior appears the same along both scanning directions. A similar investigation has been reported elsewhere [30] for a diamond detector having the same "body-centered-rectangular" 3D-cell of Fig. 1, with a pillar distance of about 280 µm and pillar diameter ranging from 30 µm (inner buried-end) to 50 µm (surface top-end). In that case, Raman analysis, performed in the region within two nearest neighbor pillars, evidenced an upshift ($v_D - v_{D0}$) of about 2.5 cm^{-1} for the diamond peak position, *i.e.* the presence of a compressive stress around 1 GPa. Comparing the two structures, it is worth to note that: *i)* a smaller pillars distance should increase crystal strain; *ii)* a smaller pillar diameter should reduce stress. The experimental results observed for the detector here investigated would underline that pillar diameter dominates in crystal strain. The effect induced by pillars diameter reduction is also clearly reported by Murphy *et al.* [9]. However, laser treatment speed (50 µm/s *vs.* 0.5 µm/s of [30]) and fluence value differences, having a fundamental role on pillar structure formation, cannot be ruled out on the resulting stress within the bulk material and much work is in progress to investigate their influence.

C. *Numerical simulation of electric field strength and dark conductivity measurements*

A 3D structure reproducing six "elementary-cells" of the fabricated device was implemented in the finite element FlexPDE 5.0.4 software by setting the different conductivity values of diamond ($\sigma = 5\times10^{-14}$ S/cm) and graphite ($\sigma = 0.2$ S/cm) domains, as well as the dielectric permittivity (5.5 and 10 for diamond and graphite, respectively). Fig. 8 reports a view of simulated electric field distribution in the perpendicular device cross section along two pillars belonging to adjacent strips (S-S' dotted trace of Fig. 1) for a voltage difference of 60 V. Neglecting the tip-effect distortion near the surface and at the pillars termination, a quite homogeneous field strength between the pillars is found with values ranging from 0.2 V/µm to more than 0.5 V/µm. At the same time, electric field lines are also induced beneath the front sample side by surface graphite strips, resulting into an extension of field strength toward the central region between pillars. In the region 50 µm above the back surface, the electric field strength around 0.1-0.2 V/µm would assure a good charge collection [39], although the contribution of carrier diffusion cannot be ruled out in untreated single-crystal diamond.

Laser-induced local graphitization of bulk diamond is expected to largely affect the electronic properties of the material. Fig. 9(a) shows the log-log plot of dark current-voltage characteristics acquired by means of a Keithley 6517A for the detector biased up to 200 V. For a bias voltage V_a up to few tens of Volts the device depicts an ohmic behavior, whereas it shows an exponential increase of the current amplitude at higher voltages. In agreement to a field-assisted detrapping process [40], such a behavior is compatible to the presence of defects acting as traps mainly located inside and in the vicinity of laser-formed graphitic contacts where a thickening of the electric field lines is also observed (see Fig. 8). As shown in Fig. 9(b), the dark conductivity *I/V* displays an exponential dependence on $V^{1/2}$ for $V > 25$ V, suggesting the onset of a classical Frenkel-Pool (FP) mechanism. Conversely, for $V_a < 30$ V, conductance remains rather constant, without any evidence of non-linear effects. It is worth to observe that the FP-plot of Fig. 9(b) highlights the presence of two different onsets, to be probably attributed to the presence of two-mains shallow traps located near the edge of extended band stated. Such a phenomenon, not observed previously [30], may be attributed to: *i)* the relatively higher fluence used for buried contacts realization; *ii)* buried-columns reduced section (able to enhance the electric field strength in close proximity of the contacts at the same applied voltages); *iii)* superficial ArF-treatment able to introduce electronic-active defects mainly located at the device surface. Although results illustrated in the following sections highlight good performance of the realized device at relatively low bias voltages, further investigations are necessary to reduce electronic-active defects induced by the overall laser-process here used for device contacts fabrication.

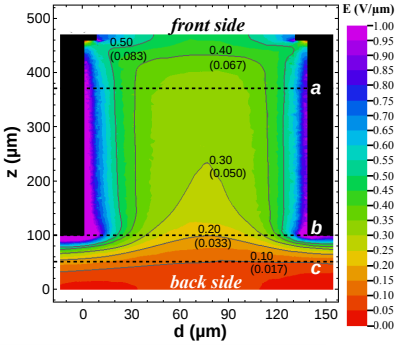

Fig. 8 Simulation results of the electric field strength distribution (at $V_a = 60$ V) along the plane S-S' of fig. 1(a). Equipotential perimeters are indicated to highlight the field distribution, and values corresponding at $V_a = 10$ V are provided between brackets. Dotted lines refer to significant depths of the device (see text).

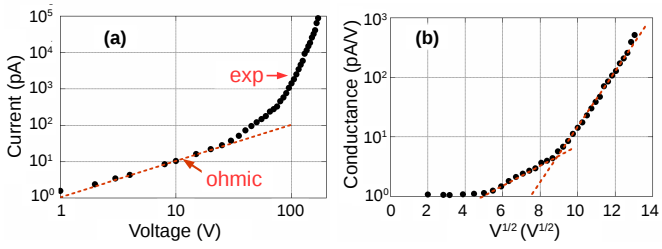

Fig. 9 (a) Current-voltage characteristics of the detector. The ohmic behavior is observed for applied bias voltages < 30 V. At higher voltages, an exponential increase of current is clearly found. In (b), logarithmic plot of *I/V* vs. $V^{1/2}$ (Frenkel-Poole plot). Two onsets of the Frenkel-Pool regime are observed, around 25 V and 60 V of the applied bias voltage.

D. *Response to MeV energy electrons*

Preliminary characterization of the detector was performed under MeV-energy electrons emitted by a ^{90}Sr source by means of the setup described in Section II.C. The device bias voltage was fixed to 10 V in order to evaluate detector

This article has been accepted for publication in a future issue of this journal, but has not been fully edited. Content may change prior to final publication. Citation information: DOI 10.1109/JSEN.2019.2939618, IEEE Sensors Journal

performance limited by the volume defined by pillars' depth (about 370 µm). Indeed, by results of simulation of the electric field distribution, for a voltage of 10 V the electric field strength in most of the volume located in the last 100 µm of the sample, where buried contacts are absent, is lower than 0.05 V/µm (see values between brackets of Fig. 8). Assuming for a "detector grade" CVD-diamond sample a mobility-lifetime $\mu\tau \sim 10^{-5}$ cm^2 V^{-1} [28], such an electric field would assure a charge-carrier drift around 50 µm, not enough to collect generated carriers at buried graphitic columns terminations.

The ^{90}Sr β-source emits low-energy electrons by the ^{90}Sr to ^{90}Y decay (end-point energy of 0.546 MeV), whereas the following ^{90}Y to ^{90}Zr decay produces electrons with an average energy of 939 keV and an end-point energy at about 2.28 MeV. The latter particles get across the whole diamond DUT, 470 µm thick, releasing part of their energy and, finally, produce a signal in the ADII-3 detector used to enable the acquisition of DUT signal. Conversely, low energy β-particles, completely absorbed in diamond, are not able to produce any charge in the back trigger detector and then the signal produced in the DUT is not acquired and processed by electronics chain. As also demonstrated by Monte Carlo simulations (Casino 2.51) performed for a monochromatic electron-source of 1.1 MeV and shown in Fig. 10(a), more than 90% of impinging particles release their energy within the 470 µm of diamond thickness. The remaining 10% get across the plate thickness, and besides, only a small fraction of them maintains the original impinging direction. Then, for the ^{90}Sr β-source we expect events recording only for particles emitted by ^{90}Y to ^{90}Zr decay, being their energy higher than the threshold of 1100 keV [41]. Events distribution versus the collected charge, reported in Fig. 10(b), shows a mean value $\langle Q_{coll} \rangle = 2.05 \pm 0.05$ fC for the collected charge, peaked at about 1.91 fC (Most Probable Value). For a rough estimation of results, let's consider such high energy β-particles as "Minimum Ionizing Particles"-like (MIPs-like). The generation rate of 36 e-h/µm for MIPs electrons [35, 42] gives a $Q_G = 2.13$ fC value of generated charge carriers within the detector thickness of about 370 µm. By $CCE = \langle Q_{coll} \rangle / Q_G$ relationship, a collection efficiency around 96% is estimated, in agreement to what expected for the high-quality diamond sample used in this work ($CCE > 95\%$ [28]). Such results confirm the effectiveness of the adopted buried-columns geometry as previously predicted in [29]. In addition, compared to other solutions where either superficial metal contacts or multi-wire bonding are implemented [9, 27, 29-30], the proposed laser direct-writing of contacts largely simplifies the fabrication of an all-carbon diamond-based device for beta-particles detection.

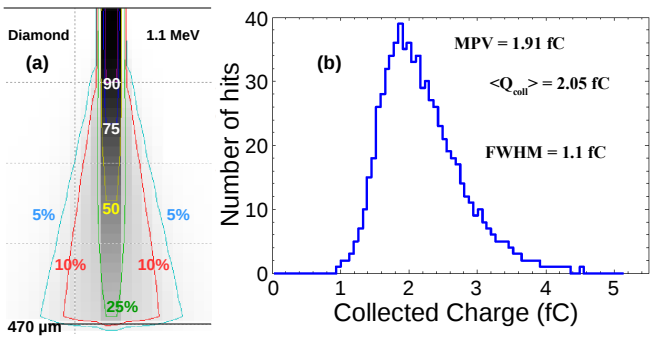

Fig. 10 (a) Cross-section view of absorbed energy in 470 µm of diamond simulated with 1100 keV electrons (CASINO software v2.51). Contour lines show the percentage of absorbed energy contained within the line. (b) Events distribution vs. the collected charge under β-particles emitted by ^{90}Sr source.

E. Response to MeV energy protons

Aimed at evaluating detector activity in the volume defined by pillars' length, as estimated by β-particles irradiation, IBIC characterization has been performed irradiating the device, biased at 60 V, either on the front or on the back surface. Indeed, with protons mainly releasing their energy around a depth of 97 µm (4.5 MeV) or 48 µm (3.0 MeV), IBIC analysis allowed to observe CCE in thin volumes located at the depths indicated as dotted lines in Fig. 8: for protons impinging on the detector front side, CCE mainly refers to a volume where pillars are embedded (dotted line '*a*'); when back irradiation is concerned, IBIC maps refer to regions at pillars termination or within a non-contacted bulk (lines '*b*' and '*c*', respectively).

Fig. 11(a) reports a map acquired irradiating a 300×300 µm^2 area of the front surface of the detector with 4.5 MeV protons (see inset). The acquisition mainly reflects the collection efficiency of charges generated about 100 µm below the sample front side. The color distribution homogeneity of the image reflects wide regions (92% of the investigated area) with an almost constant CCE around 90%. Worth to observe the good collection efficiency found in the areas where both Raman analysis and optical microscopy highlight strained regions extending for tens of microns (see Figs. 3 and 5). Buried contact positions are visible as blue-black colored dots representing a completely blind region equal to 1-2% of the total active area. At the same time a dramatic decrease of CCE, down to 60-70%, is found at about 10 µm wide pillar surroundings, where both optical microscopy and Raman spectroscopy show large stress signatures. Laser-treatment induced stress then influences CCE only close to the pillar itself, while further in the diamond bulk CCE is barely affected, as already reported [30]. This confirms the effectiveness of direct-laser-writing of diamond if compared, for example, to DIBL in which residual damages strongly affect the electronic properties of bulk material overlaying the buried-contacts structure [5].

In order to confirm that the detector active volume extents at a depth defined by pillars length, IBIC measurements were repeated irradiating the diamond detector on the back side. Fig. 11(b) shows the CCE map in a 250×250 µm^2 area under 4.5 MeV protons. In such a case, due to the depth of Bragg's peak of such protons, the generation of charge carriers is observed in a thin volume including the pillars terminations. Notwithstanding that the image shows the presence of wider regions of low CCE located around the pillars position, experimental results demonstrate a full activity of buried contacts. The acquisition now reflects a low homogeneity in the CCE distribution: wide diamond areas (60%) with CCE > 70% and low CCE around the pillars (in about a 20 µm domain size surrounding the pillars). Hence, almost blind-

This article has been accepted for publication in a future issue of this journal, but has not been fully edited. Content may change prior to final publication. Citation information: DOI 10.1109/JSEN.2019.2939618, IEEE Sensors Journal

regions now extents up to 5% of the investigated area. Such a behavior probably reflects variations induced by pillars resistivity and length able to create an electric field distortion on the volume where carriers are generated.

Finally, Fig. 12 reports a 400×200 μm^2 IBIC map obtained using 3.0 MeV protons, again irradiating the detector from its back side. Being ~47 μm the stopping range in diamond of 3 MeV protons, back irradiation involves untreated pristine diamond. However, electric field strength is high enough in most of the region giving a CCE around 60%. On the other hand, wide areas around pillars position exhibit a lower CCE, slightly higher than 20%, addressing the possibility to collect generated carriers, but with a relatively low efficiency.

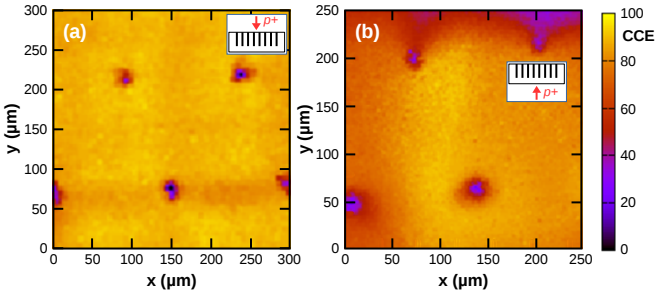

Fig. 11 (a) IBIC map of a 300×300 μm^2 area of the sample biased at 60 V. 4.5 MeV protons beam impinges on the top side of the detector (inset). (b) IBIC map of a 250×250 μm^2 area of the detector biased at 60 V. 4.5 MeV protons impinges on the back side of the device (inset).

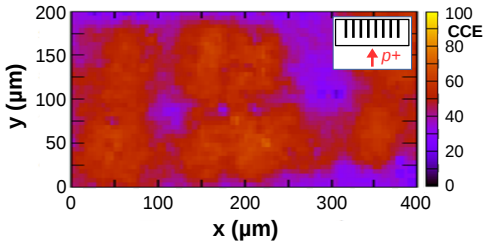

Fig. 12 IBIC map of a portion of the explored area with 3.0 MeV protons back irradiation (inset).

IV. Conclusions

Presently, the possibility to design detectors with a 3D-contact architecture, based on laser-induced transformation of insulating diamond into conducting graphite inside the bulk material and on the diamond surface, opens the way to fabricate diamond devices with sophisticated geometry which can easily be customized and adapted to the specific application, including position sensitive particle detectors and X-ray imaging [43]. In this work, graphitic conductive pillars fabricated in the bulk of a single crystal CVD diamond sample by femtosecond infrared laser and superficial graphitic strips by ArF excimer laser allowed the realization of an *all-carbon* detector having an interdigitated contacts structure and showing good performance under MeV energy particles irradiation. Moreover, the two lateral laser-formed graphic contacts largely simplified device mounting on a PCB holder, avoiding the need of wire bonding. Chosen laser scan speed, as well as fluence, allowed to realize well defined buried columns. Dark-conductivity measurements have been used to investigate the presence of electronic-active defects induced by laser-treatment. A Frenkel-Pool transport-mechanism is observed and tentatively attributed to traps located in regions close to contacts edges where electric field strength is more intense, too. In addition, polarized optical microscopy and confocal micro-Raman spectroscopy investigations highlight stress development and structural disorder on a micrometer scale at the pillar periphery and between the buried columns electrodes. In the pillar area the structural modification promoted by laser irradiation reveals graphitic sp^2 bonded carbon intermixed with highly defected sp^3 bonded diamond, as evidenced by a linewidth broadening and downward shifting of the diamond peak. Within the pillar surrounding the diamond peak gradually recover its characteristics of crystalline counterpart. At the same time, a compressive stress build up at the boundary with untreated diamond, owing to the volume expansion in the pillar area. Within the untreated diamond, the stress gradually relaxes towards an equilibrium value, which depend on the relative spatial distance of laser-formed buried electrodes, but leaving unaltered the crystalline quality of diamond.

Notwithstanding the presence of structural and point defects induced by diamond-to-graphite laser writing, device characterization under β-particles irradiation points out an almost full-charge collection of generated carriers along the detector contacts-thickness at a relatively low applied bias voltage. In addition, IBIC technique was used to evaluate mapping of charge collection efficiency, showing that most of the active volume preserves good detection properties, largely decaying close to the laser-treated zones occupied by buried electrodes. For an applied bias voltage of 60 V, under 4.5 MeV protons, a CCE value around 90% is found and uniformly distributed in the regions between buried columns, wheres it decreases down to 70% in a 10 μm pillar surrounding. IBIC maps obtained for impinging protons on the back side of the detector demonstrate a full activity of buried contact, in agreement to what argued under β-particles irradiation.

Acknowledgment

The Authors wish to thank the assistance of E.E. Ashkinazi and G. Della Ventura for access to optical microscopy with polarized light.

References

[1] E. Fretwurst, "Recent advancements in the development of radiation hard semiconductor detectors for S-LHC", Nucl. Instr. Meth. Phys. Res. A 552 (2005) 7-19.

[2] N. Venturi et al., "Results on radiation tolerance of diamond detectors", Nucl. Instr. Meth. Phys. Res. A 924, 241 (2019) 241-244.

[3] D. Asner, et al., "Diamond pixel modules", Nucl. Inst. and Meth. in Phys. Res. A 636 (2011) S125-S129.

[4] S. I. Parker, C. J. Kenney, and J. Segal, "3D - A proposed new architecture for solid-state radiation detectors", Nucl. Instr. and Meth. in Phys. Res. A 395 (1997) 328-343.

[5] J. Forneris, V. Grilj, M. Jakšic, A. Lo Giudice, P. Olivero, F. Picollo, N. Skukan, C. Verona, G. Verona-Rinati, E. Vittone, "IBIC characterization of an ion-beam-micromachined multi-electrode diamond detector", Nucl. Instr. and Meth. in Phys. Res. B 306 (2013) 181–185.

[6] M. De Feudis, V. Mille, A. Valentin, O. Brinza, A. Tallaire, A. Tardieu, R. Issaoui, J. Achard, "Ohmic graphite-metal contacts on oxygen-terminated lightly boron-doped CVD monocrystalline diamond", Diamond and Relat. Mater. 92 (2019) 18-24.

[7] P. Olivero, J. Forneris, M. JakšicÂ, Z. Pastuovic, F. Picollo, N. Skukan, E. Vittone, "Focused ion beam fabrication and IBIC characterization of a diamond detector with buried electrodes", Nucl. Instr. Meth. Phys. Res. B 269 (2011) 2340-2344.

[8] B. Caylar, M. Pomorski, P. Bergonzo, "Laser-processed three dimensional graphitic electrodes for diamond radiation detectors", Appl. Phys. Lett. 103 (2013) 043504.

[9] S. Murphy, M. Booth, L. Li, A. Oh, P. Salter, B. Sun, D. Whitehead, and A. Zadoroshnyj, "Laser processing in 3D diamond detectors", Nucl. Instr. and Meth. in Phys. Res. A 845 (2017) 136-138.

[10] M. Girolami, L. Criante, F. Di Fonzo, S. Lo Turco, A. Mezzetti, A. Notargiacomo, et. al, "Graphite distributed electrodes for diamond-based photon-enhanced thermionic emission solar cells", Carbon 111 (2017) 48–53.

[11] F. Bachmair, L. Bni, P. Bergonzo, B. Caylar, G. Forcolin, I. Haughton, D. Hits, H. Kagan, R. Kass, L. Li, et al., "A 3D diamond detector for particle tracking", Nucl. Instr. and Meth. in Phys. Res. A 786 (2015) 97-104.

[12] E. Alemanno, M. Martino, A. Caricato, M. Corrado, C. Pinto, S. Spagnolo, G. Chiodini, R. Perrino, and G. Fiore, "Laser induced nano-graphite electrical contacts on synthetic polycrystalline CVD diamond for nuclear radiation detection", Diamond and Relat. Mater. 38 (2013) 32-35.

[13] S. Lagomarsino, M. Bellini, C. Corsi, F. Gorelli, G. Parrini, M. Santoro, and S. Sciortino, "Three-dimensional diamond detectors: Charge collection efficiency of graphitic electrodes", Appl. Phys. Lett. 103 (2013) 233507.

[14] M. Komlenok, A. Bolshakov, V. Ralchenko, V. Konov, G. Conte, M. Girolami, P. Oliva, S. Salvatori, "Diamond detectors with laser induced surface graphite electrodes", Nucl. Instr. and Methods in Phys. Res. A 837 (2016) 136–142.

[15] P. Oliva, S. Salvatori, G. Conte, A. P. Bolshakov, V. G. Ralchenko, "Diamond detectors with graphite contacts", in *Advances in Sensors Review*, vol. 5th, S.Y.Yurish ed. (2018), ISBN: 9788409030386, ch. 2.

[16] J. Widner, P. Bordeaux, J. Fitz, G. De La Grange, "Laser Induced Graphite Resistors in Synthetic Diamond", Int. J. of Microcircuits and Electron. Packaging, 19 (1996) 169-178.

[17] S. Salvatori, G. Mazzeo, G. Conte, "Voltage Division Position Sensitive Detectors Based on Photoconductive Materials—Part I: Principle of Operation", IEEE Sens. J. 8(2) (2008) 188-193.

[18] B. Sun, P.S. Salter, M.J. Booth, "High conductivity micro-wires in diamond following arbitrary paths", Appl. Phys. Lett. 105 (2014) 231105.

[19] K.K. Ashikkalieva, T.V. Kononenko, E.A. Obraztova, E.V. Zavedeev, E.E. Ashkinazi, A.A. Mikhutkin, A.A. Khomich, V.I. Konov, "Nanostructured interior of laser-induced wires in diamond", Diamond and Relat. Mater. 91 (2019) 183-189.

[20] M. Girolami, A. Bellucci, P. Calvani, S. Orlando, V. Valentini, D. M. Trucchi, "Raman investigation of femtosecond laser-induced graphitic columns in single-crystal diamond", Applied Physics A, 117 (2014) 143-147.

[21] G. Forcolin, V. Grilj, B. Hamilton, L. Li, M. McGowan, S. Murphy, A. Oh, N. Skukan, D. Whitehead, and A. Zadoroshnyj, "Study of a 3D diamond detector with photon and proton micro-beams", Diamond and Relat. Mater. 65 (2016) 75-82.

[22] S. Lagomarsino, M. Bellini, C. Corsi, S. Fanetti, F. Gorelli, I. Liontos, G. Parrini, M. Santoro, and S. Sciortino, "Electrical and Raman-imaging characterization of laser-made electrodes for 3D diamond detectors", Diamond and Relat. Mater. 43 (2014) 23-28.

[23] S.M. Pimenov, A.A. Khomich, I.I. Vlasov, E.V. Zavedeev, A.V. Khomich, B. Neuenschwander, B. Jaggi, V. Romano, Appl. Phys. A 116 (2014) 545–554;

[24] B. Sotillo, A. Chiappini, V. Bharadwaj, J. P. Hadden, F. Bosia, P. Olivero, M. Ferrari, R. Ramponi, P. E. Barclay, and S. M. Eaton, "Polarized micro-Raman studies of femtosecond laser written stress-induced optical waveguides in diamond", Appl. Phys. Lett. 112 (2018) 031109.

[25] A. Khomich, K. Ashikkalieva, A. P. Bolshakov, T. Kononenko, V. Ralchenko, V. Konov, P. Oliva, G. Conte, and S. Salvatori, "Very long laser-induced graphitic pillars buried in single-crystal CVD-diamond for 3D detectors realization", Diamond and Relat. Mater. 90 (2018) 84-92.

[26] P.S. Salter, M. J. Booth, A. Courvoisier, D.A.J. Moran, and D.A. MacLaren, "High resolution structural characterization of laser-induced defect clusters inside diamond", Appl. Phys. Lett. 111 (2017) 081103.

[27] M.J. Booth, G.T. Forcolin, V. Grilj, B. Hamilton, I. Haughton, M. McGowan, S.A. Murphy, A. Oh, P.S. Salter, I. Sudić, N. Skukan, "Study of cubic and hexagonal cell geometries of a 3D diamond detector with a proton micro-beam", Diamond and Relat. Mater. 77 (2017) 137-145.

[28] The Element Six CVD Diamond Handbook, available on-line at https://e6cvd.com/media/wysiwyg/pdf/E6_CVD_Diamond_Handbook.pdf

[29] G. Conte, P. Allegrini, M. Pacilli, S. Salvatori, T. Kononenko, A. Bolshakov, V. Ralchenko, and V. Konov, "Three-dimensional graphite electrodes in CVD single crystal diamond detectors: Charge collection dependence on impinging β-particles geometry", Nucl. Instr. and Methods in Phys. Res. A 799 (2015) 10-16.

[30] M. Girolami et al., "Investigation with β-particles and protons of buried graphite pillars in single-crystal CVD diamond", Diamond and Relat. Mater. 84 (2018) 1-10.

[31] T.V. Kononenko, E.V. Zavedeev, V.V. Kononenko, K.K. Ashikkalieva, V.I. Konov, "Graphitization wave in diamond bulk induced by ultrashort laser pulses", Appl. Phys. A 119 (2015) 405-414.

[32] M. Jaksic, I. B. Radovic, M. Bogovac, V. Desnica, S. Fazinic, M. Karlusic, Z. Medunic, H. Muto, Z. Pastuovic, Z. Siketic, N. Skucan, T. Tadic, "New capabilities of the Zagreb ion microbeam system", Nucl. Instr. and Methods in Phys. Res. Sect. B 260 (2007) 114-118, DOI: 10.1016/j.nimb.2007.01.252

[33] J. F. Ziegler, M. Ziegler, and J. Biersack, "SRIM – The stopping and range of ions in matter (2010)", Nucl. Instr. and Methods in Phys. Res. Sect. B, 268 (2010) 1818-1823, DOI: 10.1016/j.nimb.2010.02.091

[34] G. Knoll, *Radiation Detection and Measurement*, 4th ed., John Wiley & Sons, Inc., USA, 2000, chap. 9.

[35] L. S. Pan, S. Han, and D. R. Kania, *Diamond: Electronic Properties and Applications*, Kluwer Academic, Dordrecht, 1995, chap. 10.

[36] Delly, John Gustav, "The Michel-Lévy Interference Color Chart – Microscopy's Magical ColorKey", Hooke College of Applied Sciences, Westmont, IL, (2003) https://www.mccrone.com/the-michel-levy-interference-color-chart-microscopys-magical-color-key/

[37] A. Tardieu, F. Cansell, and J. Petitet, "Pressure and temperature dependence of the first order Raman mode of diamond", J. Appl. Phys. 68 (1990) 3243-3245.

[38] M.H. Grimsditch, E. Anastassakis, M. Cardona, "Effect of uniaxial stress on the one-center optical phonon of diamond", Physical Review B I8(2) (1978) 901-904.

[39] J. Isberg, J. Hammersberg, H. Bernhoff, D.J. Twitchen, A.J. Whitehead, "Charge collection distance measurements in single and polycrystalline CVD diamond", Diamond and Related Materials 13 (2004) 872-875.

[40] J. Frenkel, "On Pre-Breakdown Phenomena in Insulators and Electronic Semi-Conductors", Phys. Rev. 54 (1938) 647-648.

[41] Dosimeter performance, http://alignment.hep.brandeis.edu/Devices/Dosimeter/Performance.html (2009), accessed: 2019-09-03.

[42] S. Zhao, *Characterization of the Electrical Properties of Polycrystalline Diamond Films*, Ph.D. Dissertation thesis, Ohio State University, 1994.

[43] M. Girolami, P. Allegrini, G. Conte, D.M. Trucchi, V.G. Ralchenko, S. Salvatori, "Diamond detectors for UV and X-ray source imaging", IEEE Electron Device Letters, 33(2) (2012) 224-226.

Stefano Salvatori (M'00) received the Ph.D. in Electronic Engineering from Università degli Studi Roma Tre, Rome, Italy. He is Associate Professor of Electronics with the Faculty of Engineering at the Università degli Studi ''Niccolò Cusano'', Rome, Italy. His research activity is mainly focused on diamond-based sensors for UV, X-ray, and particle detection, including processing and characterization of thin-film optoelectronic devices. He is primarily involved in the development of low-noise single- and multichannel front-end electronics for low-level signal sensors. He is chair of the technical committee on "Radiation and Particle Detectors" in the Italy Chapter of the IEEE Sensors Council.

Maria Cristina Rossi was born in Rome, Italy, in 1962. She received the Ph.D. in Electronic Engineering from Università degli Studi Roma ‘‘La Sapienza’’ in 1993. In 1994 she became a Research Associate at Università degli Studi Roma Tre, Rome, then becoming Associate Professor in 2006, at the same university. Her research interests include but are not limited to transport properties in nanostructured semiconductors and related electronic devices.

Gennaro (Rino) Conte teaches physics of electronic and optoelectronic devices at Università degli Studi Roma Tre, Rome. He has been researching solid-state devices for over forty years. His interests have ranged from the transport properties of amorphous silicon to the fabrication of surface channel MESFET devices on diamond. His current activity focuses on elementary particle detectors based on 3D Graphite-Diamond structures.

Taras Kononenko received the M.S. degree in applied physics and mathematics from the Moscow Institute of Physics and Technology, Russia, in 1990 and the Ph.D. degree in laser physics from the A.M.Prokhorov General Physics Institute, Moscow, in 1996. He is currently a Senior Research Scientist with the Department of Light-induced Surface Phenomenon, A.M.Prokhorov General Physics Institute, Moscow. His research interests are in the area of laser processing of materials, especially carbon-based materials like amorphous carbon films, mono- and polycrystalline diamond, and carbon fiber reinforced plastics.

Maxim Komlenok was born in Moscow, Russia in 1983. He received the B.S. and M.S. degrees in general physics from the Lomonosov Moscow State University Russia, in 2006 and the PhD degree in laser physics from Prokhorov General Physics Institute (GPI) RAS, Moscow, Russia, in 2013. Since 2013, he has been a Postdoc with the Laser Induced Surface Phenomena Department of GPI RAS, Moscow, Russia. He is the author of more than 40 papers. His research interests include laser processing and characterization of different carbon materials (diamonds, nanodiamonds, diamond like carbon films, nanotubes, graphene and graphite), spectroscopic diagnostics, and structure modification.

Andrey Khomich received the Ph.D. in solid state physics from General Physics Institute of Russian Academy of Sciences, Moscow, in 2016. Currently he is a senior researcher of the Radio Engineering and Electronics Institute of Russian Academy of Sciences, Fryazino. His research activity is focused on the optical spectroscopy of carbon materials, mainly natural and synthetic diamonds, nanodiamonds and radiation damaged diamonds.

Victor Ralchenko received the Ph.D. in Quantum Electronics from General Physics Institute of Russian Academy of Sciences (GPI RAS), Moscow, in 1989, where, currently he is the Head of Diamond Materials Laboratory. His research activity is mainly focused on CVD diamond growth and characterization, and on diamond applications for Raman laser, ionization radiation detectors, photon emitters on color centers.

Vitaly Konov is a well-known specialist in synthesis, characterization, laser processing and photonic applications of novel carbon materials (CVD diamond, single-wall carbon nanotubes and graphene).
His scientific carrier is associated with General Physics Institute, Moscow, where nowadays he is a director of Natural Sciences Center. Since 2000 V.I. Konov is a member of the Russian Academy of Sciences, in 1992 became a fellow member of the International Society for Optical Engineering – SPIE. He is a Professor at Moscow State University.